Progressive tau aggregation does not alter functional brain network connectivity in seeded hTau.P301L mice

Detrez, Jan R.; Ben-Nejma, Ines R. H.; Van Kolen, Kristof; Van Dam, Debby; De Deyn, Peter Paul; Fransen, Erik; Verhoye, Marleen; Timmermans, Jean-Pierre; Nuydens, Rony; Van der Linden, Annemie

Published in:
Neurobiology of Disease

DOI:
10.1016/j.nbd.2020.105011

Publication date:
2020

Neurobiology of Disease 143 (2020) 105011

Contents lists available at ScienceDirect

Neurobiology of Disease

journal homepage: www.elsevier.com/locate/ynbdi

Progressive tau aggregation does not alter functional brain network connectivity in seeded hTau.P301L mice

Jan R. Detrez[a,1], Inès R.H. Ben-Nejma[b,1], Kristof Van Kolen[c], Debby Van Dam[d,g], Peter Paul De Deyn[d,e,g], Erik Fransen[f], Marleen Verhoye[b], Jean-Pierre Timmermans[a], Rony Nuydens[a], Annemie Van der Linden[b], Georgios A. Keliris[b], Winnok H. De Vos[a,*]

[a] Laboratory of Cell Biology and Histology, University of Antwerp, Belgium
[b] Bio-Imaging Lab, University of Antwerp, Belgium
[c] Department of Neuroscience, Janssen Research and Development, Belgium
[d] Laboratory of Neurochemistry and Behavior, University of Antwerp, Belgium
[e] Department of Neurology, Memory Clinic of Hospital Network Antwerp (ZNA) Middelheim and Hoge Beuken, Antwerp, Belgium
[f] StatUa Center for Statistics, University of Antwerp, Antwerp, Belgium
[g] Department of Neurology and Alzheimer Center Groningen, University of Groningen and University Medical Center Groningen (UMCG), Groningen, The Netherlands

ARTICLE INFO

Keywords:
Tau pathology
hTau-P301L
Fibril seeding
Whole brain microscopy
Resting-state functional MRI
Functional connectivity

ABSTRACT

Progressive accumulation of hyperphosphorylated tau is a hallmark of various neurodegenerative disorders including Alzheimer's disease. However, to date, the functional effects of tau pathology on brain network connectivity remain poorly understood. To directly interrogate the impact of tau pathology on functional brain connectivity, we conducted a longitudinal experiment in which we monitored a fibril-seeded hTau.P301L mouse model using correlative whole-brain microscopy and resting-state functional MRI. Despite a progressive aggravation of tau pathology across the brain, the major resting-state networks appeared unaffected up to 15 weeks after seeding. Targeted analyses also showed that the connectivity of regions with high levels of hyperphosphorylated tau was comparable to that observed in controls. In line with the ostensible retention of connectivity, no behavioural changes were detected between seeded and control hTau.P301L mice as determined by three different paradigms. Our data indicate that seeded tau pathology, with accumulation of tau aggregates throughout different regions of the brain, does not alter functional connectivity or behaviour in this mouse model. Additional correlative functional studies on different mouse models should help determine whether this is a generalizable trait of tauopathies.

1. Background

Alzheimer's disease (AD) is a progressive neurodegenerative disease that is characterized by cognitive decline and memory dysfunction, together with behavioural and psychological regress. Histopathological examination of AD brain tissue reveals the presence of neurofibrillary tangles (NFTs), composed of hyperphosphorylated tau protein, and the accumulation of amyloid beta (Aβ) protein-bearing plaques (Braak and Braak, 1991). The progressive increase in NFTs follows a stereotypical spreading pattern in AD and is closely associated with neuronal loss and AD symptoms. This association is less evident for Aβ plaques, suggesting that tau dysfunction might mediate AD-related

Abbreviations: Aβ, Amyloid beta; ACA, Anterior cingulate area; AD, Alzheimer's disease; AI, Agranular insular area; BOLD, Blood oxygen level-dependent signal; CP, Caudoputamen; DG, Dentate gyrus; EPM, Elevated plus maze; FC, Functional connectivity; FDR, False discovery rate; HPF, Hippocampal formation; ICA, Independent component analysis; MC, Somatomotor areas; MRI, Magnetic resonance imaging; NFT, Neurofibrillary tangle; OF, Open field test; PIA, Passive inhibitory avoidance learning; PCA, Principal component analysis; PL, Prelimbic area; ROI, Region of interest; rsfMRI, Resting-state functional MRI; RSP, Retrosplenial area; SS, Somatosensory areas; VIS, Visual areas

* Corresponding author.
E-mail addresses: Ines.Ben-Nejma@uantwerpen.be (I.R.H. Ben-Nejma), KVKOLEN@its.jnj.com (K. Van Kolen), Debby.VanDam@uantwerpen.be (D. Van Dam), Peter.DeDeyn@uantwerpen.be (P.P. De Deyn), Erik.Fransen@uantwerpen.be (E. Fransen), Marleen.Verhoye@uantwerpen.be (M. Verhoye), Jean-Pierre.Timmermans@uantwerpen.be (J.-P. Timmermans), Rony.Nuydens@uantwerpen.be (R. Nuydens), Annemie.VanDerLinden@uantwerpen.be (A. Van der Linden), Georgios.Keliris@uantwerpen.be (G.A. Keliris), Winnok.DeVos@Uantwerpen.be (W.H. De Vos).
[1] joint first authorship

https://doi.org/10.1016/j.nbd.2020.105011
Received 6 January 2020; Received in revised form 21 June 2020; Accepted 7 July 2020
Available online 10 July 2020

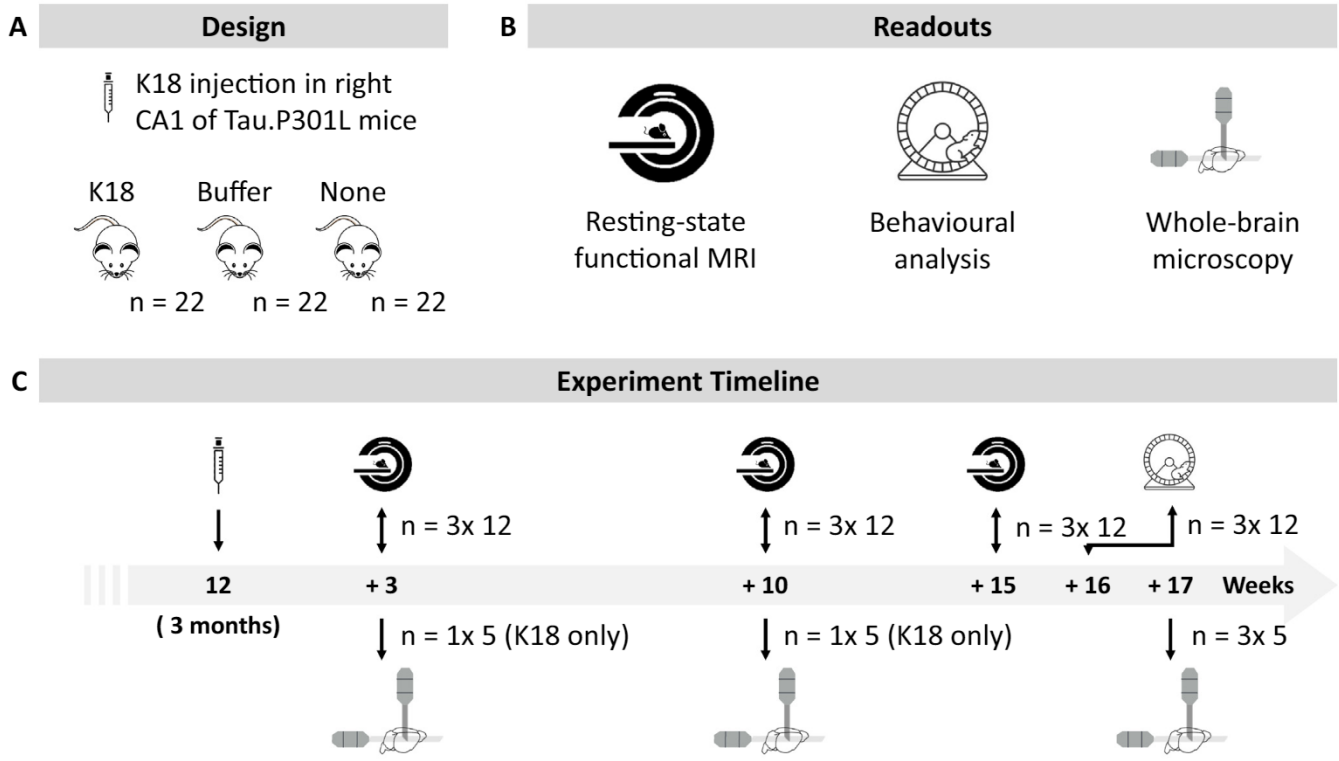

Fig. 1. Overview of the experimental setup. A. Twenty-two mice were randomly attributed to 3 experimental groups, receiving either K18 injection, buffer injection or no injection. B. Multiple readouts were derived from longitudinal MRI follow-up, a behavioural evaluation, and post-mortem whole brain microscopy. C. Time-line of the experimental setup per condition.

neurodegeneration (Bejanin et al., 2017; Kametani and Hasegawa, 2018).

The main function of tau is to stabilize microtubules in neurons. In AD and other tauopathies, tau becomes hyperphosphorylated, causing its dissociation from microtubules and the formation of tau fibrils that aggregate to NFTs (Arendt et al., 2016). This process, further referred to as tau pathology, impairs vital cellular functions, including cell polarization and axonal transport, leading to synaptic degeneration (Yoshiyama et al., 2013). Experimental studies in mouse models have revealed that sonicated tau fibrils, when injected in the brain, serve as seeds for hyperphosphorylation and aggregation of endogenous tau, which subsequently spreads through interconnected neuronal networks (Iba et al., 2013, 2015; Detrez et al., 2019). Exactly these short fibrillary forms of tau are considered to be the most toxic and are held responsible for inducing mitochondrial and synaptic dysfunction (Guerrero-Muñoz et al., 2015; Konijnenberg et al., 2015; Shafiei et al., 2017). Moreover, they are associated with disrupting cellular processes involved in memory and cognition, as measured by electrical recordings (Lasagna-Reeves et al., 2012; Stancu et al., 2015). However, the extent to which fibril-seeded tau pathology contributes to the disruption of neuronal functioning at the level of the brain networks has only been investigated to a limited extent (Ahnaou et al., 2017).

Resting-state functional MRI (rsfMRI) allows non-invasive interrogation of functional brain network connectivity (Scholvinck et al., 2010). It is based on measuring changes in the blood oxygen level-dependent (BOLD) signal in subjects at rest (*i.e.,* not performing any task), thus revealing resting-state brain networks. Multiple studies reported functional connectivity (FC) alterations in AD patients who display only mild cognitive impairment (Sheline and Raichle, 2013). While most AD patients are reported to show decreased FC, increases in FC have been documented as well (Badhwar et al., 2017). This might be explained by a bimodal effect, in which an early phase of hyperactivity is followed by hypoactivity (Jack et al., 2013). While this effect might be attributed to the presence of different Aβ conformers and neuronal compensation mechanisms (Jones et al., 2011), recent clinical evidence indicates that FC changes in AD also depend on the level of hyperphosphorylated tau in the brain (Schultz et al., 2017).

The preclinical value of rsfMRI has recently been established in rodents, demonstrating FC changes in multiple Aβ mouse models (Bero et al., 2012; Shah et al., 2013, 2016b, 2018; Grandjean et al., 2014). FC changes have also been investigated in 3xTG mice with tauopathy (APP.KM670/671NL, hTau.P301L (4R0N), PS1.M146V) (Liu et al., 2018; Manno et al., 2019). Regional homogeneity analysis revealed hyperconnectivity in young mice, a stage at which mice display tau pathology with a minimal amount of Aβ pathology. However, the presence of both tau and Aβ pathology precluded isolating the unique effect of tau pathology on FC. Moreover, it is not known to which extent the observed effect at an early time point is related to the persistent overexpression of mutant tau, or rather to the accumulation of hyperphosphorylated tau aggregates (*i.e.,* tau pathology). To further disentangle the effect of tau pathology on FC, we have injected hTau.P301L mice (hTau.P301L, 2N4R) with a truncated form of human P301L tau (K18), which locally induces tau pathology that progressively spreads to connected brain networks (Detrez et al., 2019). We performed a longitudinal study to assess how this affects functional brain connectivity measured by rsfMRI. Despite histologically overt tau pathology, no major functional changes were observed as compared to controls. In line with this, no behavioural changes were witnessed. These results suggest that seeded tau pathology does not induce detectable functional deficits in brain networks of this mouse model.

2. Methods

2.1. Animals and experimental design

hTau.P301L (2N4R) homozygous mice (Terwel et al., 2005) were

maintained on an FVB genetic background. All mice were housed in enriched cages with a 12 h light/dark cycle and access to food and water supplied ad libitum and with cage enrichment. Animals used in seeding studies were single housed and 66 animals were randomised per treatment group at the age of 3 months, *i.e.*, 22 non-injected animals, 22 buffer controls, 22 K18 injected animals (Fig. 1; totalling 66 animals). FVB mice are known to occasionally display stereotypic circling behaviour (Smith and Usherwood, 2019). Mice strongly displaying this trait were excluded from the MRI study ($n = 4$). The same was done for some animals that showed repetitive head movement during EPI recordings ($n = 3$) or demonstrated aberrant low frequency signals in the EPI ($n = 1$). Where possible, these mice were swapped with those scheduled for microscopy analysis. This way, the study consisted of min. 11 animals per group per time point (Additional file 1: Fig. S1). All experiments were performed in accordance with protocols approved under ECD files 2017–92 (University of Antwerp) and 628-Tau Spread (Janssen Pharmaceutica).

2.2. Tau fibril generation and stereotactic seeding

Generation of synthetic K18 fibrils and stereotactic seeding were performed as previously described (Detrez et al., 2019). Briefly, a truncated form of human tau with the P301L mutation containing only the four microtubule-binding repeats (K18) was produced in *Escherichia coli* (Tebu-bio) and was incubated in 133 μM heparin (MP Biomedicals 02101931) before being resuspended in PBS at 5 μg/μl and sonication (Branson probe sonicator, amplitude 15%, total sonication time was 2 min in pulses of 2 s with 10 s intervals). Prior to stereotactic seeding, mice were deeply anaesthetised with isoflurane (2% in 36% oxygen; IsoFlo, Abbott) and fixed in a stereotactic frame (Neurostar). Dipodolor (0.25 mg/kg; Janssen-Cilag) was administered via subcutaneous injection, and Xylocaine (AstraZeneca) was locally applied on the skull. A 30G syringe (Hamilton) was used for injecting 2 μl into the right hemisphere at a speed of 0.25 μl/min at the selected coordinates: anterior-posterior −1.83 and medial-lateral +1.29 from the bregma, and dorsal-ventral +1.7 from the dura.

2.3. Microscopy and image analysis

Mice were deeply anaesthetised by intraperitoneal injection (Nembutal, 150 mg/kg), following transcardial perfusion with heparinised PBS (Sigma H3393-50KU; 10 U/ml; 5 min) and 4% paraformaldehyde (Affymetrix USB. J19943; 5 min) at 2 ml/min. Brains were dissected, hemisected and post-fixed overnight in 4% PFA at 4 °C, followed by a PBS wash (3 × 15 min).

For whole-brain microscopy, fluorescent labelling and clearing of brain hemispheres were done based on the iDISCO+ protocol (Renier et al., 2016). Hyperphosphorylated tau was specifically detected using a mouse AT8 antibody (pSer202/Thr205/PSer208, produced at Janssen Pharmaceutica). This antibody was pre-labelled with a near-infrared fluorescent tag (PerkinElmer VivoTag 680XL) following the manufacturer's protocol. Cleared mouse hemispheres were imaged on an Ultramicroscope II (Lavision Biotec GmbH), equipped with an Olympus MVPLAPO 2× (NA 0.50) objective lens and DBE-corrected LV OM DCC20 dipping cap. Images were recorded with a Neo sCMOS camera (Andor) at a total magnification of 1.6× and a z-step of 10 μm resulting in 4 μm × 4 μm × 10 μm voxels. Images were captured by sequentially imaging the sample with the left and right light sheet, followed by image merging through a linear blending algorithm to obtain more homogeneous image quality. For imaging, 488 nm, 561 nm and 640 nm lasers were used with 525/50 nm, 620/60 nm and 680/30 nm emission filters, respectively. Whole-brain microscopy images were analysed with an automated pipeline described before (Detrez et al., 2019). Briefly, the autofluorescence channel was aligned to a 3D light sheet reference brain atlas, and the resulting transformation vector set was used for regional analysis of the AT8 signal. The total number of detected voxels for a given brain region was calculated and expressed relative to the brain region volume (*i.e.,* regional tau load).

Synaptic markers were analysed on 100 μm tissue sections generated from contralateral brain hemispheres of 17 weeks post injection (WPI) mice. Images were recorded from five biological replicates per group, with seven regions per biological replicate, and six images per region. Tissue sections were incubated for 1 h with a permeabilising blocking buffer (containing 0.05% thimerosal (Fluka 71,230), 0.01% sodium azide, 0.3% boseral 30 T (Sigma A7284-50ML), normal horse serum, and 1% Triton X-100). Primary antibody incubation was done with GAD65/67 (rabbit, Sigma G5163) and vGLUT1 (guinea pig, Synaptic Systems 135,304) was performed overnight at room temperature in the same buffer. After rinsing in PBS, sections were incubated for 4 h with goat anti-rabbit Cy3 (Jackson ImmunoResearch 711–165-152, 1/400) and donkey anti-guinea pig Cy5 (Jackson ImmunoResearch 706–175-148, 1/400). After rinsing in PBS, sections were mounted on coverslips. Sections were imaged on a Leica SP8 a 5×/0.15 air and 63×/1.20 water-immersion lens for overview and high-resolution images, respectively. Laser excitation was at 552 nm and 631 nm, with an emission band respectively at 560–620 nm and 640–730 nm using the Acousto-Optical Beam Splitter and detection using a Leica HyD Photon Counter or photon multipliers. For both markers, synaptic staining intensity was measured above a fixed intensity threshold and a ratio between both measures was calculated.

2.4. Animal handling

An MRI imaging and anaesthesia protocol was set up for recording rsfMRI and anatomical 3D scans (Fig. 2A). MRI acquisition sessions were performed on spontaneously breathing mice under isoflurane anaesthesia. This was done at 5% for induction, 3% for animal positioning in the bed, following a gradual decrease from 2% to 0.5% before acquiring rsfMRI (Fig. 2A; Isoflo®, Abbot Laboratories Ltd., Illinois, USA), administered in a gaseous mixture of 33% oxygen (200 cc/min) and 66% nitrogen (400 cc/min). In order to acquire the rsfMRI data in a reproducible flat-skull position, the head of the mice was fixed in an MRI compatible mouse stereotactic device with a tooth bar and blunt earplugs, in which the anaesthetic gas was delivered in a nose cone. For the acquisition of the rsfMRI data, a subcutaneous (s.c.) bolus of medetomidine, an α2-agonist (Domitor, Pfizer; 0.05 mg/kg/h) was administrated 10 min after isoflurane induction. A continuous s.c. medetomidine infusion (e.g. 0.1 mg/kg/h) was started 10 min after bolus injection and isoflurane levels were gradually decreased and maintained at 0.5% at least 5 min before the rsfMRI acquisition. After the rsfMRI scans, the isoflurane concentration was increased to 2% and the medetomidine infusion was stopped for the acquisition of anatomical 3D scans. At the end of the MRI experiment, the effects of medetomidine were counteracted by injection of 0.05 mg/kg atipamezole (Antisedan, Pfizer). Respiration rate was constantly monitored using a small animal pressure-sensitive pad (MR-compatible Small Animal Monitoring and Gating System, SA instruments, Inc.). In addition, body temperature was monitored via a rectal probe and was held constant at 37.0 ± 0.5 °C using warm air coupled to a feedback unit (SA instruments). Both respiration and body temperature control systems were controlled using a feedback controlled warm air system (MR-compatible Small Animal Heating System, SA Instruments, Inc.).

2.5. MRI acquisition

The imaging measurements were performed on a 7 T PharmascanMR scanner (Bruker Biospin). This system was equipped with a Bruker cross coil setup with a transmit quadrature volume coil and a receive-only surface array for mice. The system was interfaced to a Linux PC running Topspin 2.0 and Paravision 6.0.1 software (Bruker Biospin). A localiser scan was performed to ensure that the brain was in the centre of the magnet. Field maps were acquired for each animal to

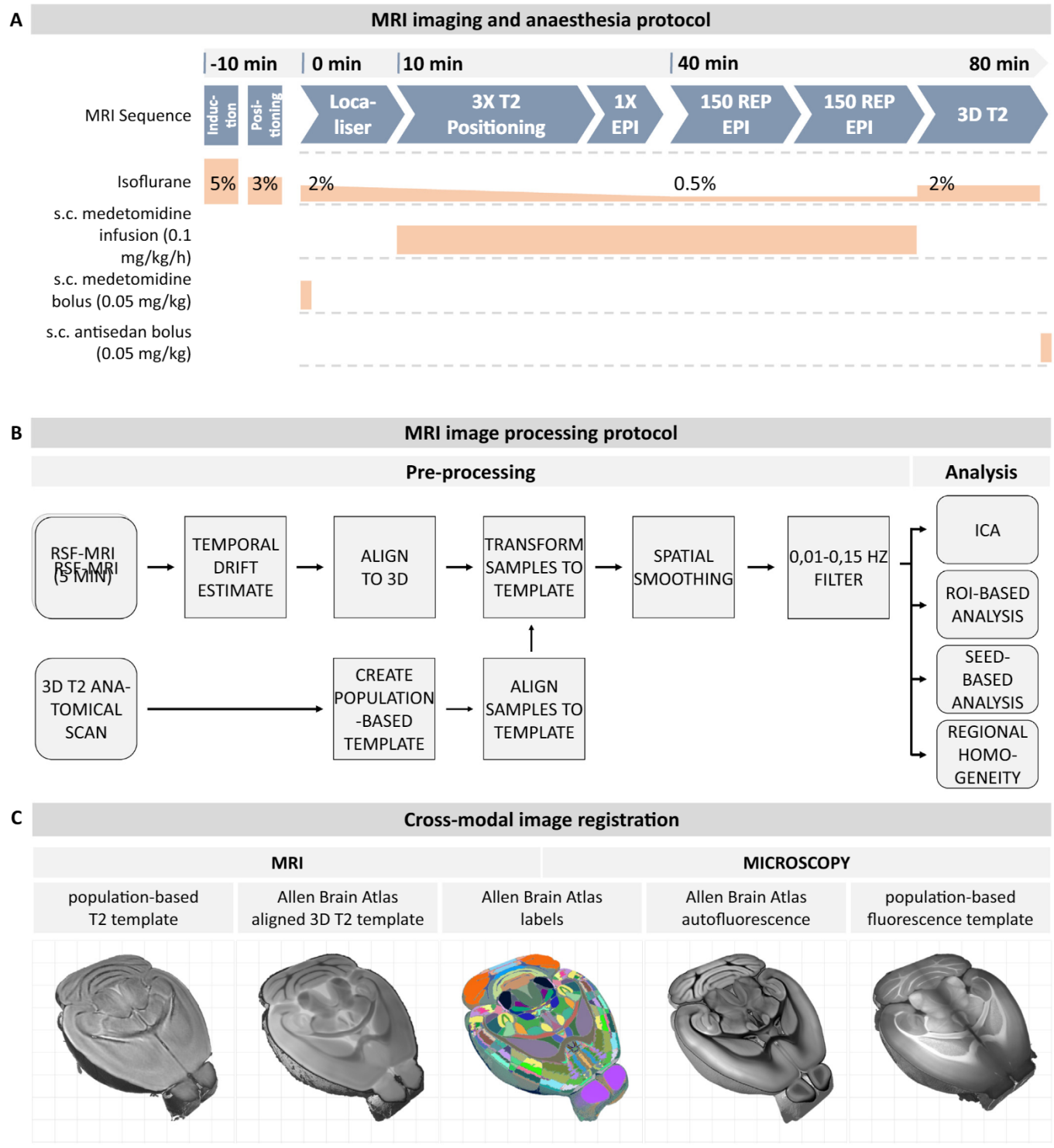

Fig. 2. A. Following anaesthesia induction, mice were placed in the MRI scanner, and the slice package was positioned. Anaesthesia was gradually decreased to the start of the rsfMRI scans 40 min after bolus injection. After rsfMRI, the anaesthesia was increased again to record the 3D T2 anatomical scan. B. rsfMRI images and 3D scans were pre-processed before aligning samples to a population-based template, following spatial smoothing and temporal filtering. rsfMRI traces were analysed with a ROI-based analysis, seed-based analysis, and independent component analysis (ICA). C. Cross-modal image registration allows direct comparison of tau load with changes in FC. This is achieved by registering the T2 MRI and light sheet population-based template to the Allen Brain Atlas. Inverse alignment of the atlas and its anatomical labels allows measuring FC and tau load, respectively. Abbreviations used: echo planar imaging (EPI), repetitions (REP) subcutaneous (s.c).

assess field homogeneity, followed by shimming in an ellipsoid region of interest confined to the brain, which corrects for the measured heterogeneity. To ensure a uniform slice positioning, three orthogonal 2D multi-slice Turbo RARE T2 images were acquired (repetition time (TR) 2500 ms, echo time (TE) 33 ms, field of view (FOV) 20 × 20 mm^2 with matrix size 256 × 256, 9 slices of 0.7 mm with 0.3 mm gap, voxel size 0.078 mm × 0.078 mm × 0.700 mm, RARE factor = 8) Saturation slices were positioned over the eyes and ventral to the brain. A single

gradient echo planar imaging (EPI) sequence was acquired, followed by two sets of 150 EPI datasets over a total time of 10 min (TR 2000 ms, TE 17 ms, FOV 20 × 20 mm^2 with matrix size 96 × 64, 12 slices of 0.4 mm with a gap of 0.1 mm, voxel size 0.208 × 0.313 × 0.400 mm^3). Only the second 150 EPI dataset was used for analysis, except for when animal movement was detected in the recording, in which case the first recording was used. We have assessed a putative effect of using the first over the second EPI on absolute FC values, but did not detect a significant effect of this factor in a mixed model analysis (not shown). Finally, a 3D anatomical scan was acquired with a Turbo RARE T2 sequence (TR 2000 ms, TE 9.66 ms, FOV 20 × 20 mm^2 with matrix size 192 × 256, 32 slices of 0.4 mm, voxel size 0.104 × 0.078 × 0.400 mm^3).

2.6. MRI image pre-processing and analysis

In the image processing pipeline (Fig. 2B), the Bruker image file format was first converted to the NIfTI file format. A population-based template was then generated by aligning all 3D anatomical scans of the 15 WPI time points to one mouse in ANTS (Avants et al., 2010), from which an average 3D temporal projection was created. Three-dimensional scans were then aligned to this template using affine registration in SPM 12 (https://www.fil.ion.ucl.ac.uk/). The temporal drift was estimated in the rsfMRI scans in SPM12, and those that exceeded twice the voxel size were excluded from analysis. The same software was used for correcting the remaining temporal drift and for aligning the rsfMRI scans to their corresponding 3D scans (*i.e.,* co-registration), followed by transforming the rsfMRI scans to the template using the 3D registration vectors. Scans were then smoothened with a 2D Gaussian filter with a full-width half maximum of twice the voxel size (0.416 × 0.626 mm^2). This step was followed by temporal filtering in RESTplus using a band-pass filter with cut-off frequencies 0.01–0.15 Hz to extract low frequency oscillations that contribute to the rsfMRI signal (Tong et al., 2019). Only the last 140 out of 150 repetitions were analysed to reject initial signal fluctuations.

Three different approaches were used to analyse MRI data sets: independent component analysis (ICA), region of interest (ROI)-based analysis, and seed-based analysis. For ICA, Gaussian smoothed rsfMRI recordings from the entire experiment were subjected to spatial ICA in GIFT to distinguish functionally connected brain networks (v4.0a; http://mialab.mrn.org/software/gift/index.html). First, the mean image intensity at every time point was subtracted. Then, a two-step data principal component analysis (PCA) was performed, in which a subject-level PCA was followed by a group PCA. From these reduced data, 20 components were extracted via ICA using the Infomax algorithm (Bell and Sejnowski, 1995). A mask was used to limit detection of brain networks to the cerebrum. For ROI-based analysis, four-voxel-sized ROIs were delineated in the left and right hemispheres based on the detected ICA components. The temporally filtered signal was extracted per selected atlas ROI in RESTplus, and a Pearson correlation coefficient between ROIs was calculated. This coefficient was z-transformed and represented in FC matrices. Selected values within FC matrices were averaged for intra-network-level FC measures, presented as a function of mouse age in line plots and analysed with linear-mixed models. Seed-based analysis was performed by selecting ten ROIs from the ROI-based analysis in both the ipsi- and contralateral hemisphere based on prior knowledge of the AT8 pathology distribution. The temporally filtered signal of the seed ROI was extracted in RESTplus, and a multiple regression was modelled in SPM with the extracted ROI signal and the estimated motion (*i.e.*, to correct motion artefacts) as covariates. The total cluster size (defined as uncorrected $p \leq .001$ and minimal cluster size = 10 voxels) of a one-sample *t*-test was measured per subject and assessed with mixed-model analysis as described below. Regional homogeneity analysis was performed using the RESTplus toolbox. Homogeneity was measured based on coherence, measuring the connectivity of each voxel with its immediate neighbouring 27 voxels. The Allen Brain Atlas was used to measure the connectivity within brain networks.

Cross-modal image registration was achieved by mapping MRI and light sheet population-based template to annotated templates from the Allen Brain Atlas with Elastix (Fig. 2C) (Klein et al., 2010). While this allows visualization of both imaging modalities in one space, an inverse alignment was calculated to correlate FC and tau load directly. In this way, the same atlas was used for detecting tau pathology measured trough light-sheet microscopy and for annotating ROIs to extract FC-based measurements.

2.7. Behavioural evaluation

Open-field (OF) testing measures the general locomotor activity, novelty-seeking and anxiety levels in animals. Animals were measured for 10 min during the dark phase of their activity cycle in a brightly lit 50 cm × 50 cm arena. Mice always started from the same corner and were allowed 1 min of adaptation. A computerised video tracking system (Ethovision, Noldus) was used to record trajectories and calculate path length and number of entries in the centre circle or the 7 cm × 7 cm corners of the open field. Exploring the centre area of this field, rather than staying in the corner, is a measure for anxiolytic and increased exploratory behaviour (Seibenhener and Wooten, 2015).

Passive inhibitory avoidance learning (PIA) evaluates cognitive abilities and fear conditioning in mice by an aversive conditioning paradigm in a step-through box. PIA was tested in a step-through box during the dark phase of the animal's activity cycle. The step-through box consisted of a first, brightly lit compartment connected with a second, dark compartment by means of a sliding door. Mice were put in the illuminated compartment, and after 5 s the sliding door connecting both compartments was opened. Upon complete entry into the dark compartment, animals received a slight foot shock (0.3 mA, 1 s). Exactly 24 h later, the escape latency to re-enter the dark compartment was timed up to 300 s, and the percentage of animals not reaching this criterion was compared between experimental groups. Impaired memory functioning or anxiolytic behaviour impairs the inhibition to enter the dark compartment after training (Decker et al., 1990).

The elevated plus maze (EPM) is a second measure for anxiety and novelty-seeking behaviour. The EPM setup consists of a cross-shaped maze, with two open arms and two closed arms (30 cm in length, 5 cm in width, 15 cm in height for in the closed arms) and a central area (5 cm by 5 cm). At the start of the 10 min trial (EthoVision XT 7.0, Noldus), mice were placed in the central area, facing an open arm in the direction away from the experimenter. Measurements include the number of entries and amount of time spent in the open and closed arms, with more interaction with the open arm indicating an anxiolytic or higher novelty-seeking behaviour (Walf and Frye, 2007).

2.8. Statistics

For microscopic image analysis, a limited number of samples was used to confirm tau pathology induction and progression over time ($n = 5$ per condition). The small sample size motivated the choice for non-parametric testing. The Mann–Whitney *U* test and Holm–Bonferroni correction were used to compare the AT8 load of K18- or buffer-injected mice with non-injected controls in R using stats::wilcox.test().

For ROI-based analysis, FC matrices were analysed with a one-sample *t*-test per group to assess the significance of the connections in R using stats::t.test(). For the pairwise connections that were considered significant from this test, a linear mixed model analysis was conducted including all groups and timepoints of the MRI experiment using linear-mixed model analysis in R using lme4::lmer(). A model was built with time and treatment as fixed effects, an interaction term time*treatment, and study subject as random effect. If the interaction term was not significant in the model (p-value > .05), the model was recalculated

without this term. Uncorrected *p*-values and a 10% false discovery rate (FDR) threshold of the remaining effects were reported. Post-hoc analysis was carried out in R using multcomp::glht() for main effect factors and emmeans::emmeans() for interactions with Tukey correction for multiple hypothesis testing. To directly assess the differential connectivity between K18 and buffer samples in FC matrices, we carried out a two-sample t-test for the significant pairwise connections at each time point. Uncorrected p-values and a 10% FDR threshold were reported. All other statistical tests on data extracted from MRI images (*i.e.,* network-level FC, and seed-based summary statistics) were done using linear-mixed model analysis as described above. For network-level FC measures, only the significant connections were used for analysis based on the one-sample t-test described above.

For behavioural evaluation, means were compared between groups with a one-way ANOVA in R using stats::aov(), followed by a posthoc analysis with a Tukey correction using stats:: TukeyHSD(). The homoskedasticity assumption for the ANOVA was visually inspected using boxplots, and through the Levene test for homogeneity of variances in R with car::leveneTest(). Normality was assessed with stats::shapiro.test (). In case the assumptions for parametric analysis were not attained, a Kruskal-Wallis test was calculated in R using stats::kruskal.test() as indicated in the figure legend. Frequency data (e.g., the number of mice not reaching a time criterion in the PIA test) were tested using a chi-squared test in R using stats::chisq.test(). To analyse the synaptic markers, the average staining intensity was first calculated over the different fields recorded from the same region. After confirming assumptions for parametric testing, the average intensity between treatment groups was analysed with one-way ANOVA and post-hoc Tukey HSD tests. Statistical differences were indicated as follows: $0.05 > p > .01$ (*), $0.01 > p > .001$ (**), and $p < .001$ (***).

3. Results

3.1. Whole-brain microscopy reveals progressive tau pathology in seeded mouse brain

In line with our previous results (Detrez et al., 2019), targeted seeding of K18 induced AT8-positive tau pathology in the hippocampus, which progressively expanded to connected brain areas (Fig. 3A, B). Spreading within the ipsilateral and to the contralateral hemisphere was already observed at 3 weeks after injection. Regional analysis showed that the AT8 signal was highest in the cortical and hippocampus regions (Fig. 3C). While a two-fold accumulation of AT8 load was found between weeks 3 and 10 in both hemispheres, only a minor increase was observed in the contralateral hemisphere between weeks 10 and 17.

3.2. MRI reveals resting-state networks in hTau.P301L mouse brain

To ascertain the validity of the injection model for functional MRI, we first compared the overall morphology of the buffer- and K18-injected mouse brains with that of non-injected brains. Anatomical and functional scans of injected hTau.P301L mice revealed visible damage along the injection tract, which was comparable across the different time points (Additional file 1: Fig. S2). However, this damage remained localized and did not result in morphological distortions, such as fluid build-up or tissue deformation upon comparison with non-injected animals.

As an internal control, we verified whether documented brain regions with correlated FC, *i.e.,* resting-state brain networks, could be identified in the rsfMRI recordings. To this end, independent component analysis (ICA) was performed on all recordings (Additional file 1: Fig. S3). Within the selected components, brain networks including the frontal, somatosensory, somatomotor, hippocampal and visual networks were detected. Thus, we conclude that morphological deformations were limited to the injection tract in this seeded mouse model, and that functional MRI can be used to detect resting-state brain networks.

3.3. Induced tau pathology does not alter major resting-state network strength

To determine whether induced tau pathology altered FC in specific resting-state networks, ROI-based analysis was performed. To this end, ROIs were selected in brain networks identified by ICA (Fig. 4A; Additional file 1: Table S1). A one-sample *t*-test per group showed no significant differences in FC strength between treatment groups at week 15 (Fig. 4A), or earlier time points of this study (Additional file 1: Fig. S4A). While a linear mixed model analysis showed subtle significant differences for specific connections on time, treatment or their interaction, they no longer met significance after applying a 10% FDR correction (Additional file 1: Fig. S4B; Additional file 1: Table S2).

When FC was analysed within the ROIs of individual brain networks (*i.e.,* intranetwork FC; Fig. 4B; Additional file 1: Table S2), only the ACA network displayed a weak interaction ($p = .022$) between time and treatment. However, post-hoc testing did not reveal any significant effects. No interaction or treatment effect was observed for regions with high AT8 load, such as the HPF, RSP or VIS networks. A negative estimate for time was found for RSP, PL and HPF, suggesting decreased FC in the hTau.P301L model irrespective of the treatment.

Because mixed-model analysis over all treatment groups did not reveal overt FC differences between treatment groups, we investigated whether focusing our analysis on the differential FC between K18 and buffer would reveal subtler differences (Fig. 5A). While this revealed a mixture of hypo- and hyperconnectivity, these differences were not consistent between the different time points, and no longer met significance after 10% FDR correction.

A previous study demonstrated that differences in FC correlated with the presence of hyperphosphorylated tau in a 3xTg tau overexpression model (Liu et al., 2018). To investigate this possibility for seeded tau pathology, we directly correlated AT8 load as measured by whole-brain microscopy with the intranetwork differential FC between K18 and buffer (Fig. 5B, C). We did not observe a significant correlation between both parameters suggesting there is no association between seed-induced tau load and FC changes.

In summary, neither mixed model analysis nor focused analysis revealed overt FC differences in K18 seeded animals. Although a correlation was found between tau load and FC, this was not consistent between time points or between hemispheres.

3.4. Seed-based connectivity and regional homogeneity do not differ between treatment groups

To discover changes in FC for a specific brain region without making a priori assumptions regarding the connections to a ROI, we next performed seed-based analysis. A total of ten ROIs was chosen as seed regions based on their abundance of AT8 load (Fig. 6A; Additional file 1: Table S2). Then, per treatment group a set of significantly connected voxels was determined, as illustrated for the R-CA1 seed in Fig. 6B. The volume of the seed-connected clusters did not significantly depend on the treatment (neither an interaction for time and treatment, nor a direct effect for treatment) for any of the chosen seeds (Fig. 6C). In line with ROI-based analysis, we did observe a negative effect of time on FC for all seeds.

To assess whether there were local differences in FC synchronization, regional homogeneity analysis was performed, which is based on the coherence between neighbouring voxels. Coherence maps were generated per subject and were displayed per treatment group (Fig. 7A). Coherence was measured for 12 brain regions in each hemisphere, but none showed an interaction between time and treatment, nor a treatment effect (Fig. 7B; Additional file 1: Table S2). In line with the ROI-based analysis, a time effect was observed for a subset of brain regions.

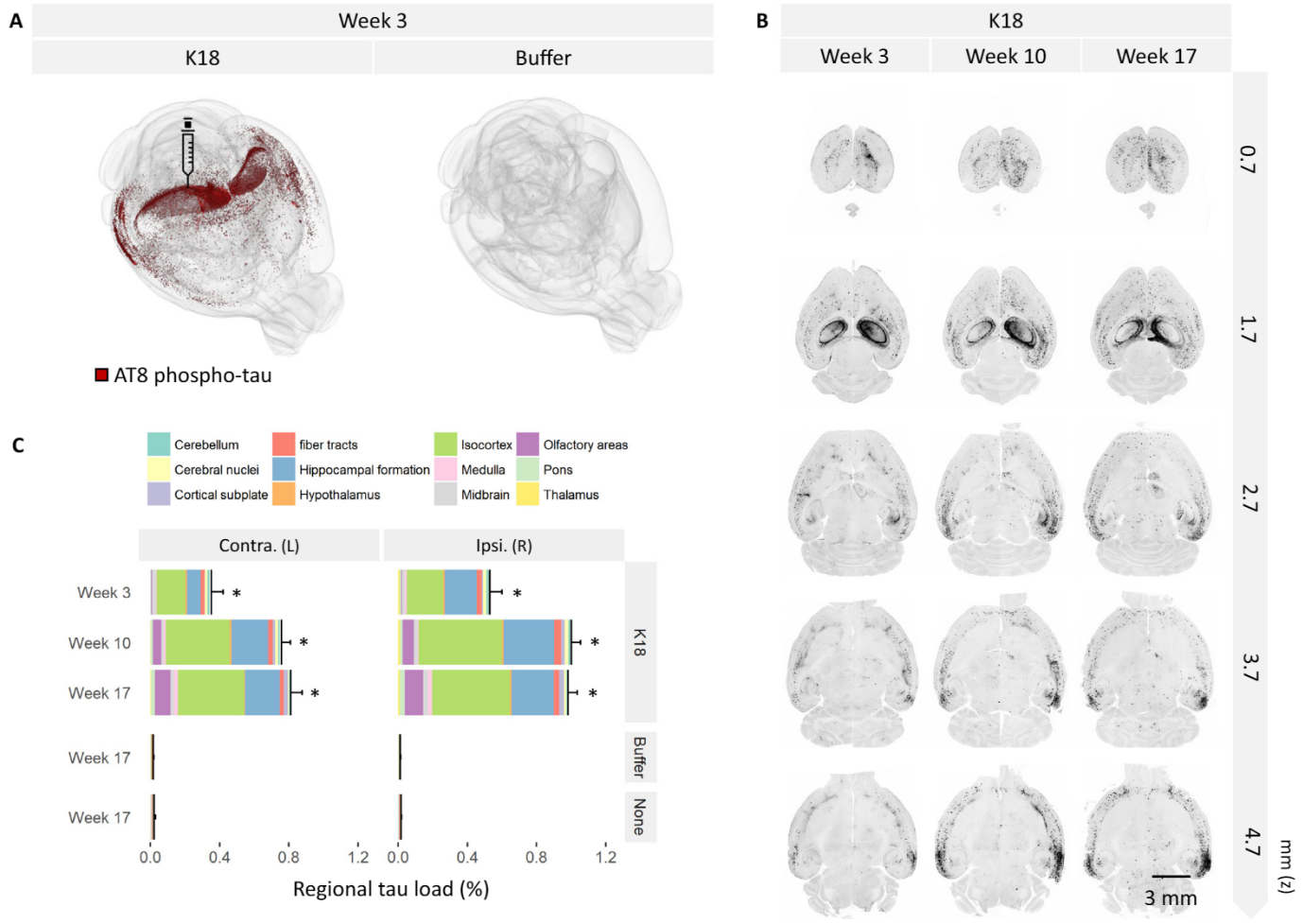

Fig. 3. Whole-brain microscopy of optically cleared hTau.P301L mouse brain reveals progressive accrual of tau pathology (labelled with an AT8 antibody) after K18 seeding. A. Rendering of a 3D image data set showing the distribution of hyperphosphorylated tau (red) 3 weeks post-injection (injection site indicated with syringe). B. Axial cross-sections at different positions within the brain showing AT8 tau pathology distribution. C. Region-specific analysis of tau pathology. Bar graphs show mean ± SEM of total AT8 tau load with colours representing regional AT8 tau load per brain region. (For interpretation of the references to colour in this figure legend, the reader is referred to the web version of this article.)

rsfMRI results indicated no major effect of K18-seeded tau pathology on brain network function. In line with this result, post-hoc quantitative immunofluorescence analysis of brain tissue for excitatory and inhibitory synaptic markers demonstrated limited differences across treatment groups (Additional file 1: Fig. S5). Only for the CA3 region a strong difference ($p < .001$) was found between the injected and none-injected group for GAD65–67, resulting in a decrease in excitatory to inhibitory staining ratio. While a difference was also detected between the K18- and buffer-injected group, the effect was limited without correcting for the number of comparisons ($P = .041$).

3.5. K18-seeded animals do not show behavioural deficits

Approximately two weeks after the last MRI measurement (*i.e.,* at 17 weeks post injection), 36 animals were subjected to behavioural evaluation. Behavioural tests were chosen to assess memory function, fear conditioning (PIA) and anxiety levels (EPM, OF) as tau pathology was abundantly present in brain regions mediating this behaviour (e.g., hippocampus and amygdala). During the PIA training phase, K18 animals were slightly slower to move from the light to the dark compartment compared to buffer controls (Fig. 8). However, no differences were observed at the testing phase, indicated by a similar latency between K18- and buffer-injected animals, and the same number of animals passing the 180 s and 300 s criterion. The K18 group spent more time in the open arms of the EPM and showed a lower latency to first enter the centre circle followed by slightly more entries in this area in OF. Although the overall results indicate a tendency towards an anxiolytic phenotype in the K18 group, no statistical difference between the K18 and buffer group could be detected.

4. Discussion

The progressive build-up of amyloid and tau pathology in the brain are major hallmarks of AD. While alteration in resting-state brain connectivity has been found in patients (Badhwar et al., 2017), it is still unclear which role both proteins play in this process. While Aβ had been suggested to be responsible for disrupting connectivity, recent clinical evidence indicates that FC changes are also depend on the level of hyperphosphorylated tau in the brain (Schultz et al., 2017). While various amyloid mouse models display changes in resting-state functional networks that are also observed in AD patients (Bero et al., 2012; Shah et al., 2013, 2016b, 2018; Sheline and Raichle, 2013; Grandjean et al., 2014; Manno et al., 2019), the picture is currently less clear for tauopathy models (Liu et al., 2018; Green et al., 2019). While tau overexpression is suggested to induce FC changes, such changes seem independent of tau hyperphosphorylation and aggregation (Green et al., 2019).

To further unravel the effect of tau pathology on FC impairment, we

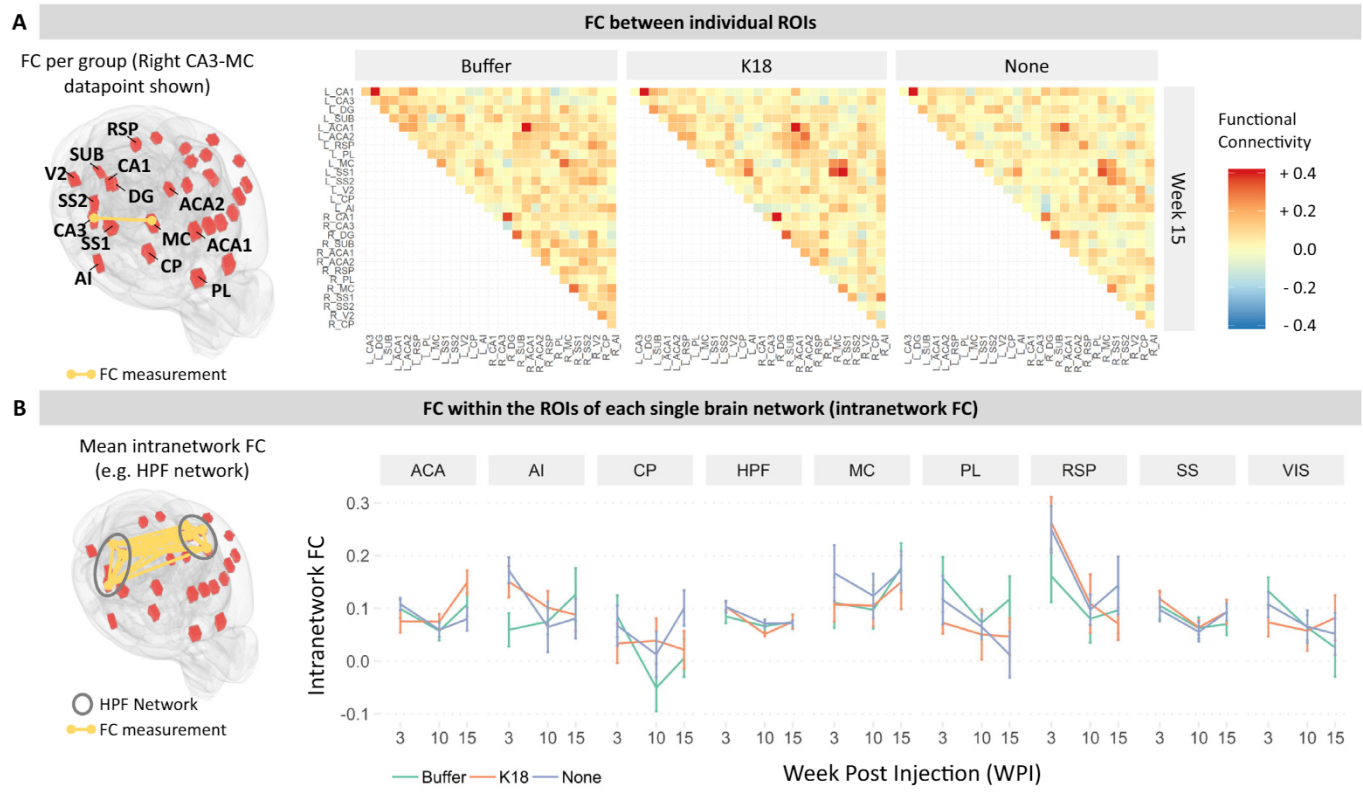

Fig. 4. ROI-based analysis does not reveal significant differences between groups. A. 3D rendering indicates all ROIs selected for ROI-based analysis. Left and right ROIs are extracted separately. An FC matrix showing the FC per treatment group is shown on the right. B. The intra-network FC represent a measure FC within brain networks. The intra-network FC calculated by averaging the FC of all ROIs within each brain network with grouping done according to Additional file 1: Table S1. The mean intra-network FC is visualised per group, time-point and within 9 brain network. Line plots represent mean ± SEM, and parameter *p*-values for mixed-model analysis are displayed in Additional file 1: Table S2.

performed a longitudinal study in which functional brain connectivity was monitored with rsfMRI in a seeded tau mouse model. Whole-brain microscopy confirmed progressive tau pathology following K18 seeding, as well as the virtual absence of hyperphosphorylated tau in controls. As documented before, K18 seeded tau pathology displays early (AT8) and late-stage tau pathology development (AT100/p-FTAA) (Detrez et al., 2019). The limited increase in seed-induced tau pathology between week 10 and week 17 indicates that a plateau of tau pathology development was reached at our final time point. We have previously established that activated, rod-like microglia are present at this stage, which are considered to beimportant mediators of tau-induced neurotoxicity (Detrez et al., 2019; Shi et al., 2019). We did not detect synaptic changes at the last time point of this study. This indicates that despite seed-induced brain-wide tau pathology development and a corresponding inflammatory response, synaptic connectivity is not dramatically altered by tau seeding within the time window of this study.

Apart from a persistent lesion around the injection site, no major anatomical deformations were observed. To exclude possible confounding effects of this lesion, ROI-based measurements were not performed in the proximity of this tract, and non-injected animals were included in the study to control for possible distal lesion-induced effects. Although issues with medetomidine anaesthesia in FVB mice have been reported (Ince, 2004; Chuang and Nasrallah, 2017), FVB mice were previously used in rsfMRI (Chang et al., 2018) and the rsfMRI anaesthesia protocol was validated in-house with multiple mouse strains (Shah et al., 2016a; Shah et al., 2016b; Anckaerts et al., 2019). The absolute *Z*-transformed values reported in FC-matrices are in line with previously published results of neurodegenerative and pharmacological models (Fig. S3A; Shah et al., 2015; Shah et al., 2016a; Shah et al., 2016b; Anckaerts et al., 2019). While others have described overall higher FC values in tau models (Green et al., 2019), this was described in another mouse strain with a different genetic background and at different age, which are factors known to affect this value (Shah et al., 2016a; Egimendia et al., 2019). In this respect, it must be noted that all animals used in this study overexpress human tau (Tau.P301L) which is known to reduce overall FC (Green et al., 2019). In addition, the use of different preprocessing steps (e.g. detrending, spatial smoothing, temporal filtering) precludes a direct comparison of absolute FC values between studies. Furthermore, it was demonstrated that key resting-state networks could be extracted with ICA, indicating that the model is amenable for rsfMRI analysis.

Apart from an effect of time, which may be attributed to progressive human tau protein deposition in the hTau.P301L mouse model (and not the induced variant) or unrelated aging factors (Egimendia et al., 2019), no significant changes in FC patterns emerged between groups. ROI-based analysis revealed subtle effects for an interaction between time and treatment, and for a main effect of treatment before correction. Similar results were observed when ROI-based FC was assessed at a network level. Nevertheless, these effects were no longer significant with a liberal 10% FDR correction, and no clear correlation was found between FC changes and the AT8 hyperphosphorylated tau load distribution. Moreover, seed-based and regional homogeneity analysis did not show evidence of a treatment effect either. This indicates that neither K18-induced tau pathology, nor the injection procedure, seems to induce overt functional changes.

While conventional tau mouse models do not allow disentangling tau overexpression from tau fibrillization, a recent rsfMRI study elegantly demonstrated that reduced FC is observed in mice overexpressing mutant human tau, but that FC is similar between tau pro-aggregant and tau anti-aggregant mice (TauRD/ΔK280 and TauRD/ΔK280/PP; Green et al., 2019). While the pro-aggregant model induces

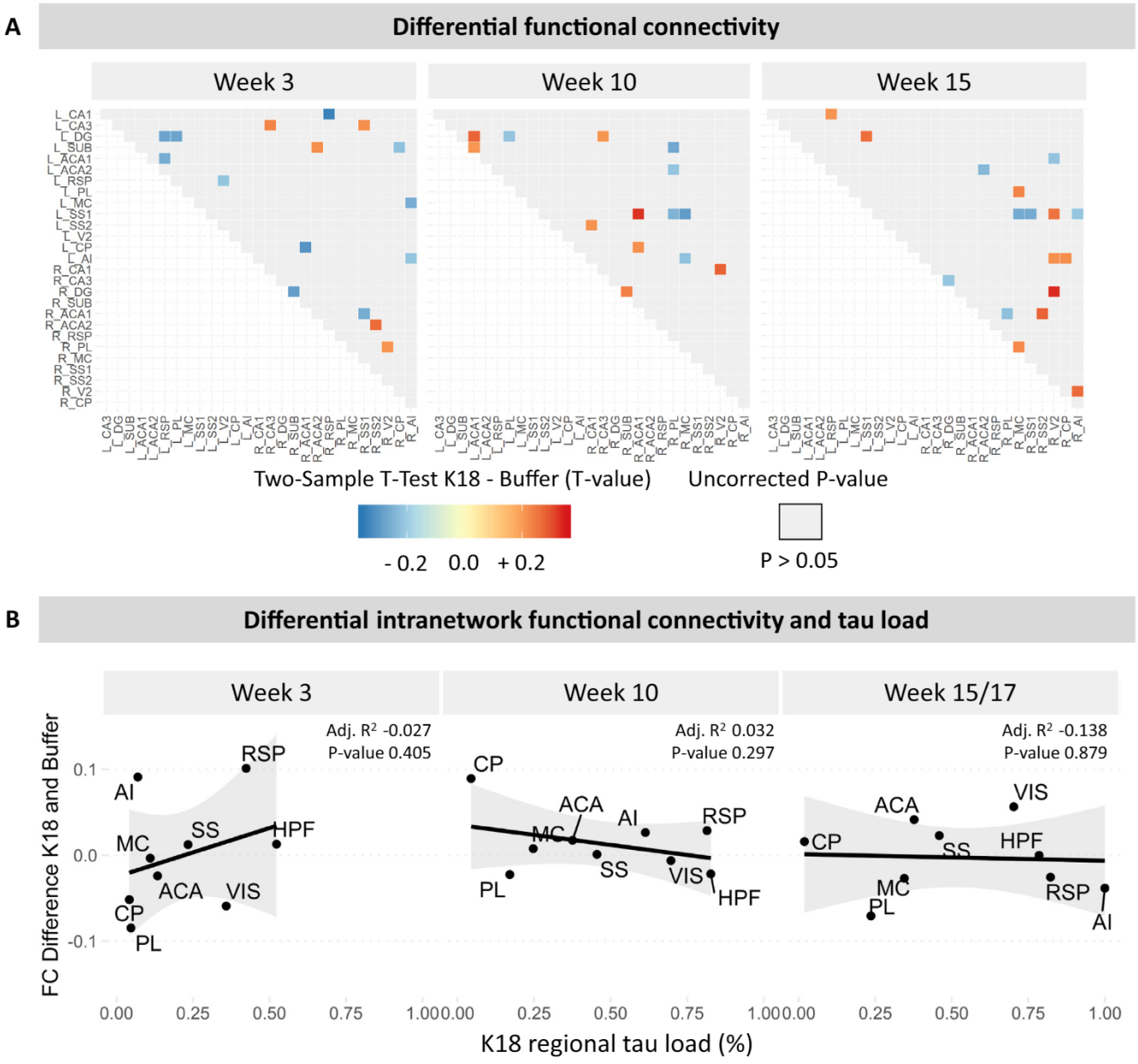

Fig. 5. Differential analysis between K18 and the buffer group does not show overt differences A. A differential FC matrix was constructed by performing a *t*-test between the K18 and buffer condition. The matrix displays uncorrected T-values for which the corresponding p-value was below 0.05. No comparisons remained after 10% FDR correction. B. The difference in intra-network FC strength (*i.e.,* the FC within brain networks) between K18 and buffer controls does not correlate with the regional AT8 load..

tau hyperphosphorylation and aggregation, its anti-aggregant counterpart merely overexpresses tau, lacking development of a pathological phenotype. This suggests that tau overexpression is sufficient to induce FC deficits, independent of its aggregation state. In line with this, our study demonstrates that tau seeding, which induces tau hyperphosphorylation and aggregation (Detrez et al., 2019), does not alter FC within a time window of 16 weeks. It would be interesting to assess whether the overexpression of MAPT has a similar effect on FC in hTau.P301L as found for TauRD mice. However, this would require a new study that includes wild-type controls.

Electroencephalography (EEG) (Ahnaou et al., 2017), in a similar seeded hTau.P301L mouse model demonstrated a progressive decrease in coherent activity between the prefrontal cortex and hippocampus at 4 weeks post injection as well as EEG theta oscillations (at 8 WPI). While EEG and rsfMRI can be considered complementary brain recording tools, both modalities reflect different aspects of neuronal activity with the former detecting the electrical synchronicity neurons and the latter gauging the metabolic demand thereof. While this might partly explain diverging results, it must also be noted that the seeding protocol was different in the cited study, *i.e.,* different CA1 coordinates, dosing (25 µg cited study vs 15 µg current study), volume (5 µl cited study vs 2 µl current study) and buffer (ammonium acetate cited study vs PBS current study). A combination of these effects may have amplified functional deficits of seeded tau pathology. It would be valuable to assess the effects of tau seeding in the same mouse cohort with EEG and rsfMRI to further scrutinise the effect of tau pathology on brain network function.

At the final stage of our longitudinal study, we subjected the mice to a set of behavioural paradigms to assess memory function, fear conditioning and anxiety levels. While a tendency towards an anxiolytic

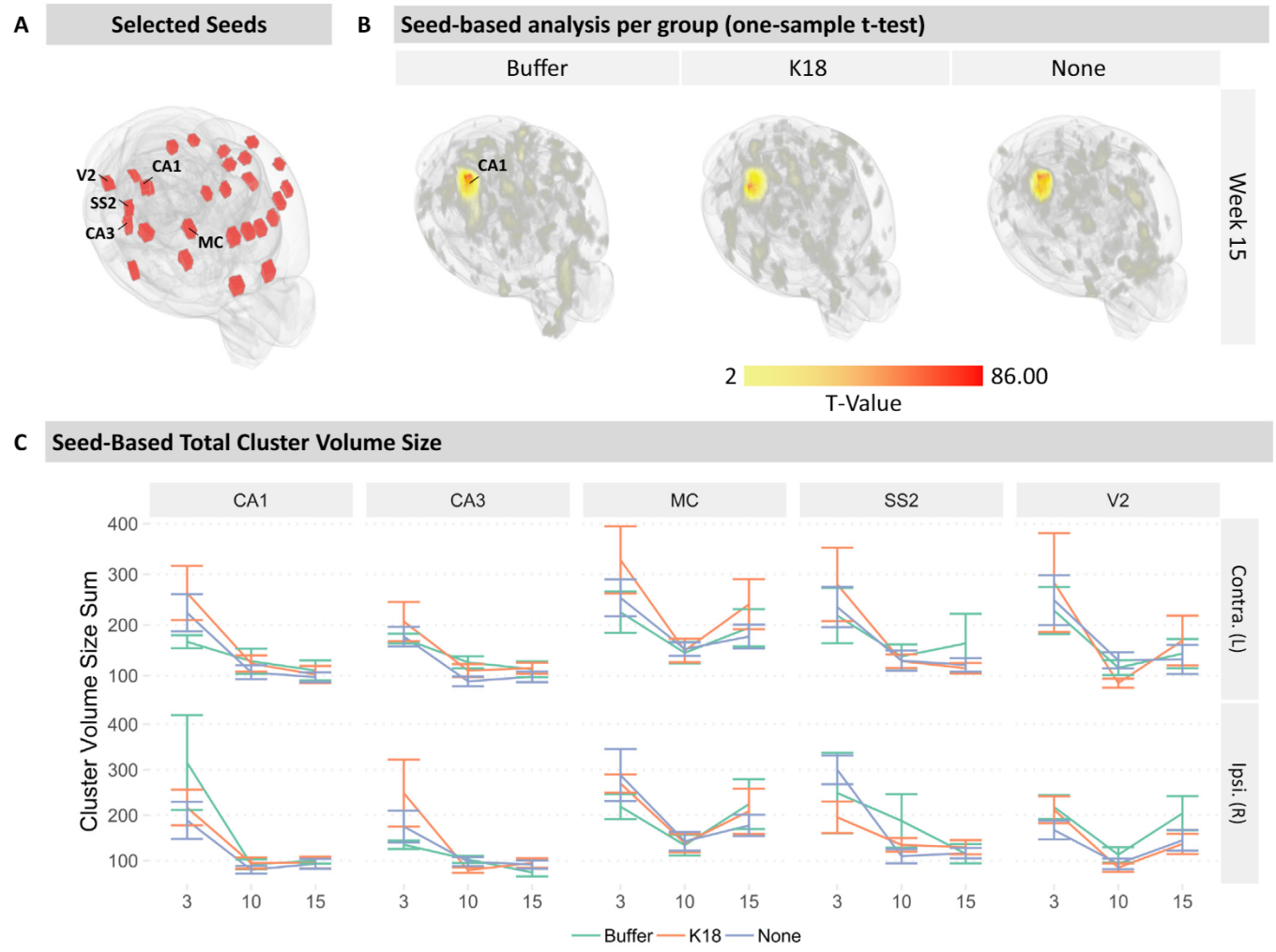

Fig. 6. Seed-based analysis does not show differences between treatment groups. A. The following ROIs were selected for seed-based analysis in the left and right hemispheres: CA1, V2, SS2, CA3 and MC B. Visual representation of T values per group for a one-sample t-test using CA1 as seed C. Per seed, the size of the connected voxel clusters was measured. This parameter did not show an interaction or treatment effect, while a time effect was found for all seeds. Line plots represent mean ± SEM, and parameter p-values for mixed-model analysis are displayed in Additional file 1: Table S2.

phenotype was observed, cognitive abilities remained unaltered in K18-injected hTau.P301L animals at 16 WPI, aged 7 months. While no behavioural studies have been conducted in seeded hTau.P301L mice to our knowledge, previous studies reported decreases in PIA and novel object recognition in hTau.P301L mice at 7 months compared to wild-type controls (Maurin et al., 2014). The results of the latter study indicate that the cognitive abilities in this model are impaired as a result of long-term overexpression of human tau, but the authors acknowledged increased variation of this effect with age. Although K18-seeding triggers extensive tau pathology compared to buffer controls, the functional effects described in the cited study may therefore have been confounded by tau overexpression, the presence of other tau pathology markers, or other undocumented age-related covariates that mediate tau function. Two other studies performed K18-seeding in hTau.P301S mice before behavioural effects resulting from overexpression became evident (Sankaranarayanan et al., 2015; Stancu et al., 2015). They revealed impaired novel object recognition test (NORT) in K18-seeded mice at 1 month (Sankaranarayanan et al., 2015) and 6 months (Stancu et al., 2015) after injection. However, the mouse model, strain, seeding protocol and behavioural testing method were different from our study. Systematic behavioural evaluation with different tau mouse models in a longitudinal design would be a valuable approach to further investigate K18-induced behavioural deterioration. Alternatively, studies have recently shown seeding in wild-type mice (Guo et al., 2016), providing a means to investigate the effect of seed-induced tau pathology in a wild-type context. As AD-derived seeds are known to trigger tau pathology at a much slower rate, such seeds might better reflect the decade-long development of tau pathology observed in humans and the correlated synaptic toxicity, neuronal loss and cognitive decline (Aisen et al., 2017). Performing such a study in a humanised model that also recapitulates other AD risk factors, including amyloid pathology and inflammatory deficits would further ameliorate the translational value of this approach (Onos et al., 2016).

5. Conclusions

We have established a correlative imaging methodology that enables interrogating functional connectivity and hyperphosphorylated tau burden in the brain of the same mouse model. Our study revealed that the accumulation of tau aggregates does not necessarily impinge on major functional connectivity networks or behaviour. This has important implications for the interpretation of results obtained with fibril-seeded mouse models but may also have broader relevance by questioning the putative adverse effect of tau aggregates altogether.

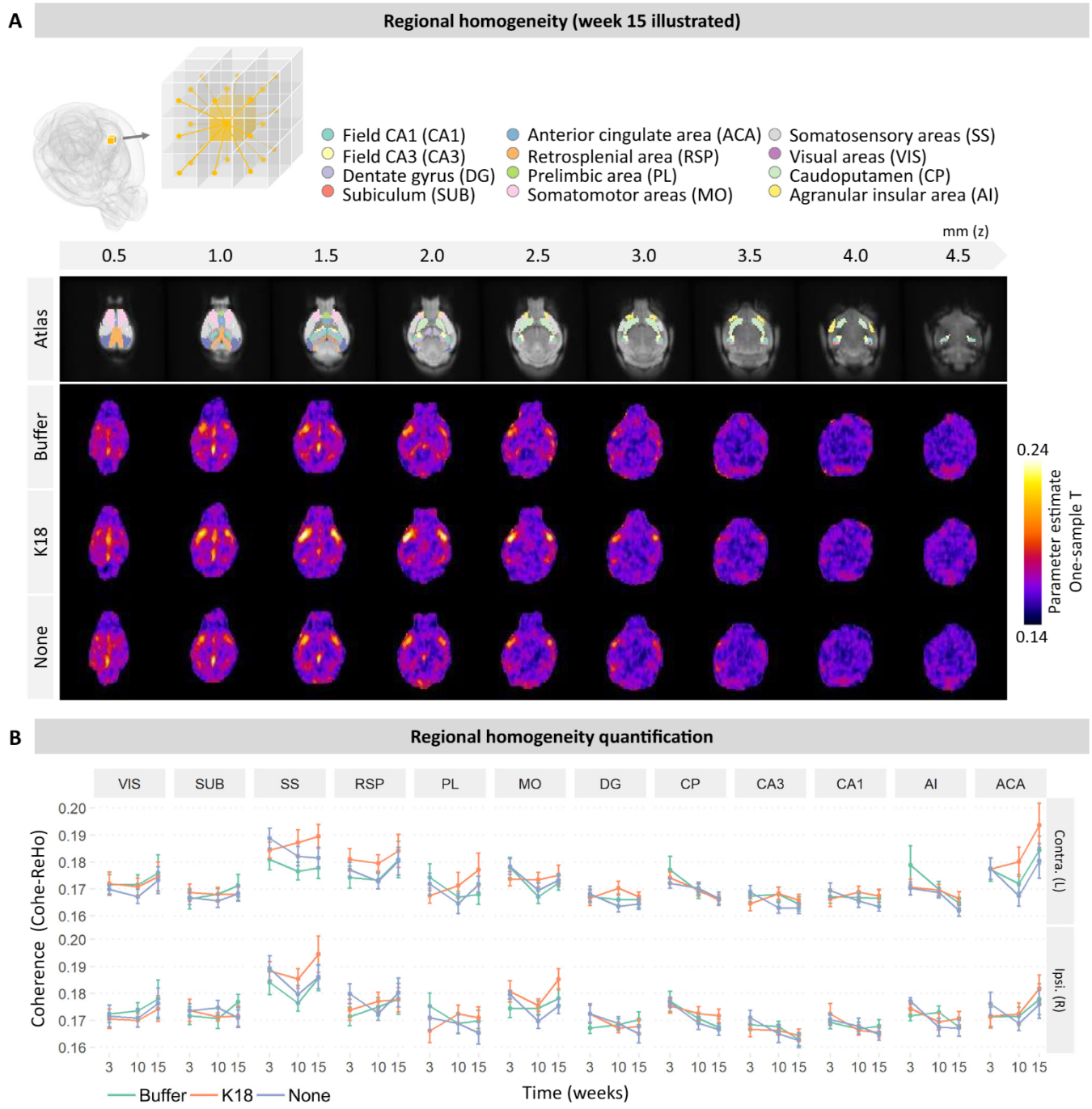

Fig. 7. Regional homogeneity analysis does not discriminate between treatment groups. A. Regional homogeneity was measured in SPM, and the Allen Brain Atlas was used to measure coherence per brain region. A one-sample t-test was performed, and the parameter estimate was visualised in a fire look-up-table. B. Quantification of the coherence signal per brain region did not show an interaction or treatment effect; only a time effect was observed. Line plots represent mean ± SEM, and parameter p-values for mixed-model analysis are displayed in Additional file 1: Table S2.

Systematic multimodal interrogation of different transgenic mouse models should allow for determining the generalizability of these observations.

Ethics approval and consent to participate

Not applicable.

Consent for publication

Not applicable.

Availability of data and materials

Part of the datasets supporting the conclusions of this article are available in the BioStudies repository, https://www.ebi.ac.uk/biostudies/studies/S-BSST304. Image and data processing scripts are available on request.

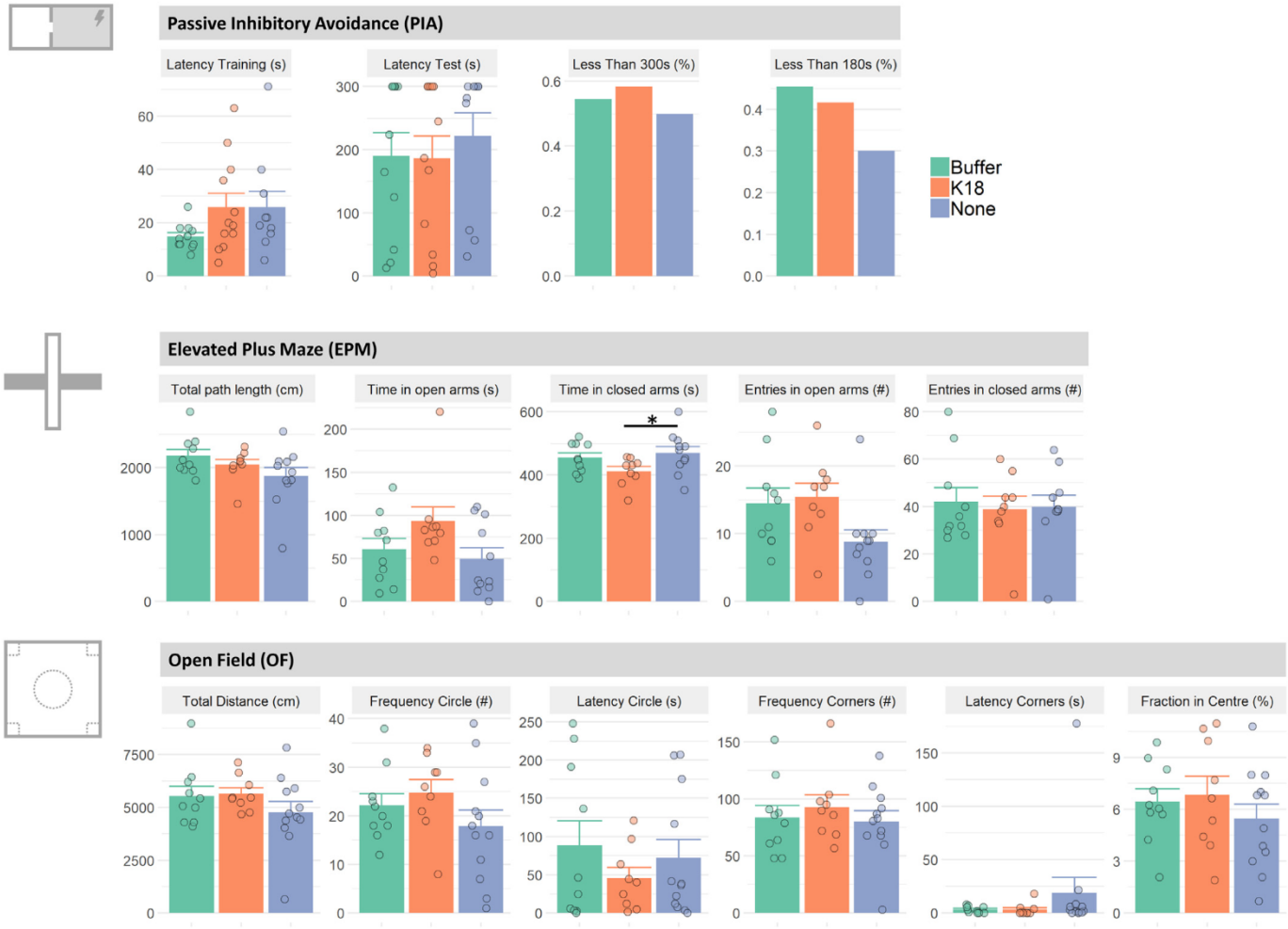

Fig. 8. Behavioural evaluation does not reveal changes in K18-injected animals. Parameters for PIA, EPM and a selection of the most relevant OPT parameters are shown. K18-injected animals do not show impaired memory function in PIA. While they show a slight anxiolytic phenotype, as evidenced by an increased time spent in the open arms of the EPM, and a lower latency to first enter the centre circle followed by more entries, no significant differences were found between the K18 and buffer group. Mean ± SEM are shown. ANOVA tests were done for all parameters as described in the methods, except for three parameters that did not meet testing assumptions for which Kruskal-Wallis tests were used (*i.e.,* for Path length (cm), Latency Circle (s), Latency Corners (s)).

Delaration of Competing Interest

JRD is mandate holder of a Baekeland grant (IWT140775) of Flanders Innovation and Entrepreneurship (VLAIO) which is a collaboration between Antwerp University and Janssen Pharmaceutica. JRD has been appointed as a fulltime employee at UCB during preparation of the manuscript. KVK is fulltime employee of Janssen Pharmaceutica as was RN at the time of the experiments.

Funding

This research was supported by a Baekeland grant (IWT140775) of Flanders Innovation and Entrepreneurship (VLAIO) and the SAO-FRA foundation (2017–0016).

Author contributions

JRD and WHDV conceived the work and wrote the manuscript. KVK prepared tau fibrils. JRD carried out the mouse surgery, histological processing, microscopic imaging and analysis. JRD and IB carried out the MRI imaging and analysis with the supervision of MV, AVDL and GAK. DVD supervised the behavioural experiments. EF provided expertise on the statistical analysis. All authors provided critical feedback on the manuscript.

Acknowledgements

We are indebted to Verdi Vanreusel, Johan Van Audekerke for technical assistance during the MRI experiments. The computational resources and services used in this work were in part provided by the HPC core facility CalcUA of the Universiteit Antwerpen, the VSC (Flemish Supercomputer Center), funded by the Hercules Foundation and the Flemish Government – department EWI.

Appendix A. Supplementary data

Supplementary data to this article can be found online at https://doi.org/10.1016/j.nbd.2020.105011.

References

Ahnaou, A., Moechars, D., Raeymaekers, L., Biermans, R., Manyakov, N.V., Bottelbergs, A., et al., 2017. Emergence of early alterations in network oscillations and functional connectivity in a tau seeding mouse model of Alzheimer's disease pathology. Sci. Rep. 7, 14189.

Aisen, P.S., Cummings, J., Jack, C.R., Morris, J.C., Sperling, R., Frölich, L., et al., 2017. On the path to 2025: understanding the Alzheimer's disease continuum. Alzheimers Res. Ther. 9, 60.

Anckaerts, C., van Gastel, J., Leysen, V., Hinz, R., Azmi, A., Simoens, P., et al., 2019. Image-guided phenotyping of ovariectomized mice: altered functional connectivity, cognition, myelination, and dopaminergic functionality. Neurobiol. Aging 74, 77–89.

Arendt, T., Stieler, J.T., Holzer, M., 2016. Tau and tauopathies. Brain Res. Bull. 126, 238–292.
Avants, B.B., Yushkevich, P., Pluta, J., Minkoff, D., Korczykowski, M., Detre, J., et al., 2010. The optimal template effect in hippocampus studies of diseased populations. Neuroimage 49, 2457–2466.
Badhwar, A., Tam, A., Dansereau, C., Orban, P., Hoffstaedter, F., Bellec, P., 2017. Resting-state network dysfunction in Alzheimer's disease: a systematic review and meta-analysis. Alzheimer's Dement (Amsterdam, Netherlands) 8, 73–85.
Bejanin, A., Schonhaut, D.R., La Joie, R., Kramer, J.H., Baker, S.L., Sosa, N., et al., 2017. Tau pathology and neurodegeneration contribute to cognitive impairment in Alzheimer's disease. Brain 140, 3286–3300.
Bell, A.J., Sejnowski, T.J., 1995. An information-maximization approach to blind separation and blind deconvolution. Neural Comput. 7, 1129–1159.
Bero, A.W., Bauer, A.Q., Stewart, F.R., White, B.R., Cirrito, J.R., Raichle, M.E., ... Holtzman, D.M., 2012. Bidirectional relationship between functional connectivity and amyloid-β deposition in mouse brain. J. Neurosci. 2012 32 (13), 4334–4340.
Braak, H., Braak, E., 1991. Neuropathological stageing of Alzheimer-related changes. Acta Neuropathol. 82, 239–259.
Chang, W.T., Puspitasari, F., Garcia-Miralles, M., Yeow, L.Y., Tay, H.C., Koh, K.B., Tan, L.J., Pouladi, M.A., Chuang, K.H., 2018. Connectomic imaging reveals Huntington-related pathological and pharmaceutical effects in a mouse model. NMR Biomed. 31 (12), e4007.
Chuang, K.-H., Nasrallah, F.A., 2017. Functional networks and network perturbations in rodents. Neuroimage 163, 419–436.
Decker, M.W., Tran, T., McGaugh, J.L., 1990. A comparison of the effects of scopolamine and diazepam on acquisition and retention of inhibitory avoidance in mice. Psychopharmacology 100, 515–521.
Detrez, J.R., Maurin, H., Van Kolen, K., Willems, R., Colombelli, J., Lechat, B., et al., 2019. Regional vulnerability and spreading of hyperphosphorylated tau in seeded mouse brain. Neurobiol. Dis. 127, 398–409.
Egimendia, A., Minassian, A., Diedenhofen, M., Wiedermann, D., Ramos-Cabrer, P., Hoehn, M., 2019. Aging reduces the functional brain networks strength-a resting state fMRI study of healthy mouse brain. Front. Aging Neurosci. 11, 277.
Grandjean, J., Schroeter, A., He, P., Tanadini, M., Keist, R., Krstic, D., et al., 2014. Early alterations in functional connectivity and White matter structure in a transgenic mouse model of cerebral amyloidosis. J. Neurosci. 34, 13780–13789.
Green, C., Sydow, A., Vogel, S., Anglada-Huguet, M., Wiedermann, D., Mandelkow, E., et al., 2019. Functional networks are impaired by elevated tau-protein but reversible in a regulatable Alzheimer's disease mouse model. Mol. Neurodegener. 14, 13.
Guerrero-Muñoz, M.J., Gerson, J., Castillo-Carranza, D.L., 2015. Tau oligomers: the toxic player at synapses in Alzheimer's disease. Front. Cell. Neurosci. 9, 1–10.
Guo, J.L., Narasimhan, S., Changolkar, L., He, Z., Stieber, A., Zhang, B., et al., 2016. Unique pathological tau conformers from Alzheimer's brains transmit tau pathology in nontransgenic mice. J. Exp. Med. 213, 2635–2654.
Iba, M., Guo, J.L., McBride, J.D., Zhang, B., Trojanowski, J.Q., Lee, V.M.-Y., 2013. Synthetic tau fibrils mediate transmission of neurofibrillary tangles in a transgenic mouse model of Alzheimer's-like Tauopathy. J. Neurosci. 33, 1024–1037.
Iba, M., McBride, J.D., Guo, J.L., Zhang, B., Trojanowski, J.Q., Lee, V.M.Y., 2015. Tau pathology spread in PS19 tau transgenic mice following locus coeruleus (LC) injections of synthetic tau fibrils is determined by the LC's afferent and efferent connections. Acta Neuropathol. 130, 349–362.
Ince, C., 2004. The Physiological Genomics of the Critically Ill Mouse. Springer Science & Business Media.
Jack, C.R., Wiste, H.J., Weigand, S.D., Knopman, D.S., Lowe, V., Vemuri, P., et al., 2013. Amyloid-first and neurodegeneration-first profiles characterize incident amyloid PET positivity. Neurology 81, 1732–1740.
Jones, D.T., Machulda, M.M., Vemuri, P., McDade, E.M., Zeng, G., Senjem, M.L., et al., 2011. Age-related changes in the default mode network are more advanced in Alzheimer disease. Neurology 77, 1524–1531.
Kametani, F., Hasegawa, M., 2018. Reconsideration of amyloid hypothesis and tau hypothesis in Alzheimer's disease. Front. Neurosci. 12, 25.
Klein, S., Staring, M., Murphy, K., Viergever, M.A., Pluim, J., 2010. Elastix: a toolbox for intensity-based medical image registration. IEEE Trans. Med. Imaging 29, 196–205.
Konijnenberg, A., Bannwarth, L., Yilmaz, D., Koçer, A., Venien-Bryan, C., Sobott, F., 2015. Top-down mass spectrometry of intact membrane protein complexes reveals oligomeric state and sequence information in a single experiment. Protein Sci. 24, 1292–1300.
Lasagna-Reeves, C.A., Castillo-Carranza, D.L., Sengupta, U., Guerrero-Munoz, M.J., Kiritoshi, T., Neugebauer, V., et al., 2012. Alzheimer brain-derived tau oligomers propagate pathology from endogenous tau. Sci. Rep. 2, 700.
Liu, D., Lu, H., Stein, E., Zhou, Z., Yang, Y., Mattson, M.P., 2018. Brain regional synchronous activity predicts tauopathy in 3×Tg AD mice. Neurobiol. Aging 70, 160–169.
Manno, F.A.M., Isla, A.G., Manno, S.H.C., Ahmed, I., Cheng, S.H., Barrios, F.A., et al., 2019. Early stage alterations in White matter and decreased functional Interhemispheric hippocampal connectivity in the 3xTg mouse model of Alzheimer's disease. Front. Aging Neurosci. 11, 1–10.
Maurin, H., Chong, S.-A., Kraev, I., Davies, H., Kremer, A., Seymour, C.M., et al., 2014. Early structural and functional defects in synapses and Myelinated axons in stratum Lacunosum Moleculare in two preclinical models for Tauopathy. PLoS One 9, e87605.
Onos, K.D., Sukoff Rizzo, S.J., Howell, G.R., Sasner, M., 2016. Toward more predictive genetic mouse models of Alzheimer's disease. Brain Res. Bull. 122, 1–11.
Renier, N., Adams, E.L., Kirst, C., Wu, Z., Azevedo, R., Kohl, J., et al., 2016. Mapping of brain activity by automated volume analysis of immediate early genes. Cell 165, 1789–1802.
Sankaranarayanan, S., Barten, D.M., Vana, L., Devidze, N., Yang, L., Cadelina, G., et al., 2015. Passive immunization with Phospho-tau antibodies reduces tau pathology and functional deficits in two distinct mouse Tauopathy models. PLoS One 10, e0125614.
Scholvinck, M.L., Maier, A., Ye, F.Q., Duyn, J.H., Leopold, D.A., 2010. Neural basis of global resting-state fMRI activity. Proc. Natl. Acad. Sci. 107, 10238–10243.
Schultz, A.P., Chhatwal, J.P., Hedden, T., Mormino, E.C., Hanseeuw, B.J., Sepulcre, J., et al., 2017. Phases of Hyperconnectivity and Hypoconnectivity in the default mode and salience networks track with amyloid and tau in clinically Normal individuals. J. Neurosci. 37, 4323–4331.
Seibenhener, M.L., Wooten, M.C., 2015. Use of the open field maze to measure Locomotor and anxiety-like behavior in mice. J. Vis. Exp. 96https://doi.org/10.3791/52434. 52434.
Shafiei, S.S., Guerrero-Muñoz, M.J., Castillo-Carranza, D.L., 2017. Tau oligomers: cytotoxicity, propagation, and mitochondrial damage. Front. Aging Neurosci. 9, 1–9.
Shah, D., Jonckers, E., Praet, J., Vanhoutte, G., Delgado Y Palacios, R., Bigot, C., et al., 2013. Resting state FMRI reveals diminished functional connectivity in a mouse model of amyloidosis. PLoS One 8, e84241.
Shah, D., Blockx, I., Guns, P.J., De Deyn, P.P., Van Dam, D., Jonckers, E., y Palacios, R.D., Verhoye, M., Van der Linden, A., 2015. Acute modulation of the cholinergic system in the mouse brain detected by pharmacological resting-state functional MRI. Neuroimage 109, 151–159.
Shah, D., Deleye, S., Verhoye, M., Staelens, S., Van der Linden, A., 2016a. Resting-state functional MRI and [18F]-FDG PET demonstrate differences in neuronal activity between commonly used mouse strains. Neuroimage 125, 571–577.
Shah, D., Praet, J., Latif Hernandez, A., Höfling, C., Anckaerts, C., Bard, F., et al., 2016b. Early pathologic amyloid induces hypersynchrony of BOLD resting-state networks in transgenic mice and provides an early therapeutic window before amyloid plaque deposition. Alzheimers Dement. 12, 964–976.
Shah, D., Latif-Hernandez, A., De Strooper, B., Saito, T., Saido, T., Verhoye, M., ... Van der Linden, A., 2018. Spatial reversal learning defect coincides with hypersynchronous telencephalic BOLD functional connectivity in APP NL-F/NL-F knock-in mice. Scientific reports 8 (1), 1–11.
Sheline, Y.I., Raichle, M.E., 2013. Resting state functional connectivity in preclinical Alzheimer's disease. Biol. Psychiatry 74, 340–347.
Shi, Y., Manis, M., Long, J., Wang, K., Sullivan, P.M., Remolina Serrano, J., ... Holtzman, D.M., 2019. Microglia drive APOE-dependent neurodegeneration in a tauopathy mouse model. Journal of Experimental Medicine 216 (11), 2546–2561.
Smith, B.J.H., Usherwood, J.R., 2019. An instrumented centrifuge for studying mouse locomotion and behaviour under hypergravity. Biol. Open. https://doi.org/10.1242/bio.043018. bio043018.
Stancu, I.C., Vasconcelos, B., Ris, L., Wang, P., Villers, A., Peeraer, E., et al., 2015. Templated misfolding of tau by prion-like seeding along neuronal connections impairs neuronal network function and associated behavioral outcomes in tau transgenic mice. Acta Neuropathol. 129, 875–894.
Terwel, D., Lasrado, R., Snauwaert, J., Vandeweert, E., Van Haesendonck, C., Borghgraef, P., et al., 2005. Changed conformation of mutant tau-P301L underlies the moribund Tauopathy, absent in progressive, nonlethal Axonopathy of tau-4R/2N transgenic mice. J. Biol. Chem. 280, 3963–3973.
Tong, Y., Hocke, L.M., Frederick, B.B., 2019. Low frequency systemic hemodynamic "noise" in resting state BOLD fMRI: characteristics, causes, implications, mitigation strategies, and applications. Front. Neurosci. 13, 787. https://doi.org/10.3389/fnins.2019.00787.
Walf, A.A., Frye, C.A., 2007. The use of the elevated plus maze as an assay of anxiety-related behavior in rodents. Nat. Protoc. 2, 322–328.
Yoshiyama, Y., Lee, V.M.Y., Trojanowski, J.Q., 2013. Therapeutic strategies for tau mediated neurodegeneration. J. Neurol. Neurosurg. Psychiatry 84, 784–795.